The Quest for Pd^{II}–Pd^{II} Interactions: Structural and Spectroscopic Studies and Ab Initio Calculations on Dinuclear [Pd$_2$(CN)$_4$(μ-diphosphane)$_2$] Complexes

Bao-Hui Xia,[a] Chi-Ming Che,*[a] and Zhong-Yuan Zhou[b]

Abstract: Structural and spectroscopic properties of and theoretical investigations on dinuclear [Pd$_2$(CN)$_4$(P–P)$_2$] (P–P = bis(dicyclohexylphosphanyl)-methane (**1**), bis(dimethylphosphanyl)-methane (**2**)) and mononuclear *trans*-[Pd(CN)$_2$(PCy$_3$)$_2$] (**3**) complexes are described. X-ray structural analyses reveal Pd···Pd distances of 3.0432(7) and 3.307(4) Å in **1** and **2**, respectively. The absorption bands at $\lambda > 270$ nm in **1** and **2** have $4d_\sigma^* \rightarrow 5p_\sigma$ electronic-transition character. Calculations at the CIS level indicate that the two low-lying dipole-allowed electronic transition bands in model complex [Pd$_2$(CN)$_4$(μ-H$_2$-PCH$_2$PH$_2$)$_2$] at 303 and 289 nm are due to combinations of many orbital transitions. The calculated interaction-energy curve for the skewed dimer [{*trans*-[Pd(CN)$_2$(PH$_3$)$_2$]}$_2$] is attractive at the MP2 level and implies the existence of a weak Pd^{II}–Pd^{II} interaction.

Keywords: ab initio calculations · metal–metal interactions · palladium · UV/Vis spectroscopy

Introduction

Studies on metal–metal interactions in homobimetallic d^8–d^8 systems[1] have generated considerable interest in inorganic and organometallic photochemistry, luminescent materials, and columnar stacking of square-planar metal complexes.[2] Extensive spectroscopic studies on dinuclear Rh^I, Ir^I, and Pt^{II} complexes have revealed weak metal–metal bonding interactions in the ground states[3, 4] and a net metal–metal single bond in $^{1,3}[(nd_\sigma^*)(n+1)p_\sigma]$ excited states produced on excitation.[5]

Compared with the numerous reports on Pt^{II} complexes, less attention has been devoted to the study of metal–metal interactions in Pd^{II} systems by spectroscopy. Many structural studies have revealed short intramolecular Pd···Pd separations, for example, 2.715(3) Å in [Pd$_2$(S$_2$CCH$_2$Ph)$_4$],[6] 2.5626(7) Å in [Pd$_2$(dpt)$_4$] (dptH = 1,3-diphenyltriazene),[7] 2.754(1) Å in [Pd$_2$(dta)$_4$] (dtaH = dithioacetic acid),[8] 2.546(1) Å in [Pd$_2$(mhp)$_4$] (mhpH = 6-methyl-2-hydroxypyridine),[9] 2.745(1) Å in [Pd$_2$(bttz)$_4$] (bttzH = 1,3-benzothiazole-2-thiol),[10] 2.570(1) Å in [Pd$_2$(chp)$_4$] (chp$^-$ = 6-chloro-2-hydroxypyridinate),[11] 2.677(1) Å in [Pd$_2$(pyt)$_4$] (pytH = pyridine-2-thiol),[12] and 2.622(3) Å in [Pd$_2$(form)$_4$] [form = (*p*-CH$_3$C$_6$H$_4$)NCHN(*p*-CH$_3$C$_6$H$_4$)$^-$].[13] Some dinuclear Pd^{II} complexes display longer Pd···Pd separations, such as 2.927(3) and 3.046(2) Å in the two diastereoisomers of [Pd$_2${4-OCH$_3$C$_6$H$_4$N=C(COPh)Ph}$_2$(μ-OAc)$_2$].[14] Furthermore, trinuclear [Pd$_3$(μ_3-S)$_2$(L)$_3$](ClO$_4$)$_2$ complexes show intramolecular Pd···Pd separations of 3.065(1) Å for L = 4,4′-*t*Bu$_2$bpy and 3.156(1) Å for L = 4,4′-(CO$_2$Me)$_2$bpy.[15] Although the Pd···Pd separations in the above complexes are shorter than or fall within the range of M···M distances found in linear-chain platinum complexes (3.0–3.5 Å),[16] the evidence for Pd^{II}–Pd^{II} interaction at separations shorter than the sum of the van der Waals radii (3.26 Å)[17] remains controversial. Cotton et al.[13] performed SCF-Xα-SW calculations on the model [Pd$_2$(HNCHNH)$_4$] with a Pd···Pd distance of 2.622 Å and concluded that there is no net Pd–Pd interaction at the "zeroth order".

Previous studies by Patterson et al.[18] on the photoluminescence of the chain compound Ba[Pd(CN)$_4$]·4H$_2$O revealed that the fluorescence at 382 nm, which was attributed to changes in intermolecular Pd···Pd separations, is strongly temperature dependent. The dinuclear complex [Pd$_2$(CN)$_4$(dppm)$_2$] (dppm = bis(diphenylphosphanyl)methane) with a Pd···Pd separation of 3.276(1) Å was previously studied in our group to probe the Pd^{II}–Pd^{II} interaction.[2b] However, the assignment of excited states with Pd–Pd bonds

[a] Prof. Dr. C.-M. Che, B.-H. Xia
Department of Chemistry
The University of Hong Kong
Pokfulam Road, Hong Kong SAR (P. R. China)
Fax: (+852)2857-1586
E-mail: cmche@hku.hk

[b] Prof. Z.-Y. Zhou
Department of Applied Biology and Chemical Technology
Hong Kong Polytechnic University
Hung Hom, Kowloon, Hong Kong SAR (P. R. China)

Supporting information for this article is available on the WWW under http://www.chemeurj.org/ or from the author.

by spectroscopic means was complicated by the intraligand transition of the dppm ligand. We have now synthesized the new dinuclear complexes $[Pd_2(CN)_4(\mu\text{-dcpm})_2]$ (**1**; dcpm = bis(dicyclohexylphosphanyl)methane) and $[Pd_2(CN)_4(\mu\text{-dmpm})_2]$ (**2**; dmpm = bis(dimethylphosphanyl)methane) and the mononuclear congener *trans*-[Pd(CN)$_2$(PCy$_3$)$_2$] (**3**). The absorption and photophysical properties of these complexes have been studied. Theoretical calculations on the $[Pd_2(CN)_4(\mu\text{-H}_2PCH_2PH_2)_2]$ and $[\{trans\text{-}[Pd(PH_3)_2(CN)_2]\}_2]$ models to probe the ground-state Pd^{II}–Pd^{II} interaction were undertaken.

Results

Syntheses and characterization: The diphosphane ligands dcpm and dmpm were chosen for the syntheses of dinuclear Pd^{II} complexes. Unlike dppm, the dcpm and dmpm ligands are optically transparent in the UV region. Therefore, it is feasible to probe high-energy metal–metal-bonded electronic transitions. We prepared $[Pd_2(CN)_4(\mu\text{-dcpm})_2]$ (**1**) and $[Pd_2(CN)_4(\mu\text{-dmpm})_2]$ (**2**) by modification of the method of Shaw et al.[19] The IR spectra show one intense $\nu(C\equiv N)$ band at 2125 and 2124 cm^{-1} for **1** and **2**, respectively, in accordance with a *trans* geometry. The $^{31}P\{^1H\}$ NMR spectra of both complexes show one set of ^{31}P signals, consistent with their formulation. Variable-temperature (20 to $-60\,^\circ$C) $^{31}P\{^1H\}$ NMR spectra showed little change in $^{31}P\{^1H\}$ chemical shift ($\Delta\delta < 1$ ppm) with temperature. However, the signal for **1** gradually broadens with decreasing temperature, and the full width at half-maximum (fwhm) is about 2 ppm at $-60\,^\circ$C (see Supporting Information). In contrast, the spectra of **2** measured at different temperatures all show single sharp peaks.

To aid spectral assignment, we prepared the monomeric congener *trans*-[Pd(CN)$_2$(PCy$_3$)$_2$] (**3**). Its IR spectrum shows one intense $\nu(C\equiv N)$ band at 2124 cm^{-1}.

X-ray crystal structures: The dinuclear complexes **1** and **2** were characterized by X-ray crystallography. The crystal data and structure refinement are summarized in Table 1. The ORTEP plots are depicted in Figures 1 and 2, and selected bond lengths and angles are listed in Table 2. Complexes **1** and **2** are structurally related to other $[M_2(CN)_4(L)_2]$ complexes (L = dcpm, dmpm, M = Pt, Ni;[2f] L = dppm, M = Pt,[2a] Pd[2b]). Complex **1** has a pseudo-C_2 symmetry, while **2** contains a crystallographically imposed center of symmetry. In both complexes, each Pd atom has a square-planar geometry with two *trans*-cyano groups and two *trans*-P atoms of bridging diphosphane ligands. The two PdP$_2$(CN)$_2$ units in **2** are eclipsed, similar to the structures of $[Pd_2(CN)_4(dppm)_2]$[2b] and other $[M_2(CN)_4(L)_2]$ (M = Pt,[2a,f] Ni;[2f] L = dppm and/or dmpm) analogues. However, the two PdP$_2$(CN)$_2$ units in **1** are not eclipsed but skewed, with the P-Pd-Pd-P and C-Pd-Pd-C dihedral angles of about 22 and 28°, respectively. As mentioned in previous work,[2f] the structural difference between dmpm-, dppm-, and dcpm-bridged metal complexes could be attributed to the steric bulk of the dcpm ligand, which disfavors an eclipsed arrangement of neighboring

Table 1. Crystal data and refinement of **1** and **2**.

Complex	**1** · 2.5 H$_2$O	**2**
formula	C$_{54}$H$_{92}$N$_4$P$_4$Pd$_2$ · 2.5 H$_2$O	C$_{14}$H$_{28}$N$_4$P$_4$Pd$_2$
M [g mol^{-1}]	1179.08	589.14
crystal system	monoclinic	monoclinic
space group	$P2/a$	$P2_1/n$
a [Å]	18.086(3)	9.067(1)
b [Å]	14.777(2)	11.533(2)
c [Å]	23.739(3)	10.618(2)
α [°]	90.0	90.0
β [°]	100.13(2)	90.623(3)
γ [°]	90.0	90.0
V [Å^3]	6245(1)	1110.3(3)
Z	4	2
$F(000)$	2484	600
μ(Mo$_{k\alpha}$) [cm^{-1}]	7.18	19.18
ρ_{calcd} [Mg m^{-3}]	1.254	1.810
$2\theta_{max}$ [°]	51.1	55.04
reflections collected	58325	7086
independent reflections	11894	2548
parameters	597	120
final R indices, $R1/wR$	0.049/0.080[a]	0.023/0.080[b]
GOF	2.42	0.69
max./min. residual electron density [e Å^{-3}]	$-$0.58/1.08	$-$0.50/0.55

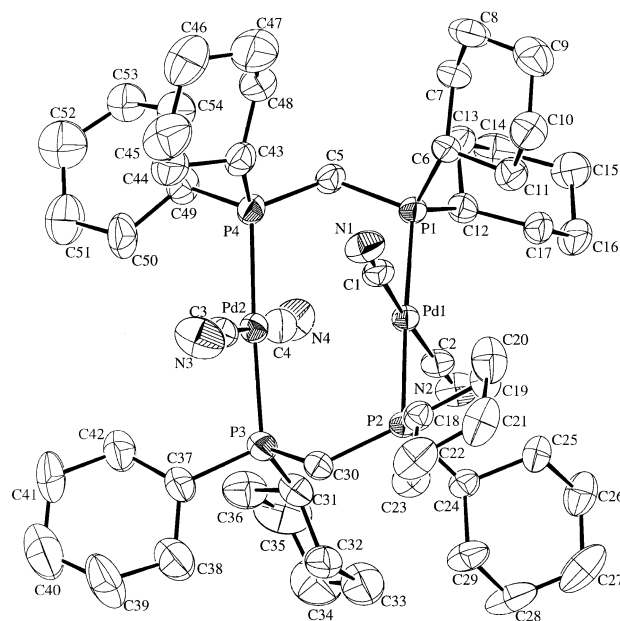[a] By least-squares refinement on F. [b] By least-squares refinement on F^2.

Figure 1. Structure of **1** (ORTEP plot: thermal ellipsoids at the 40% probability level; hydrogen atoms are not shown).

MP$_2$(CN)$_2$ moieties. The P-Pd-P angles in **1** and **2** are about 177°, while the C-M-C angles are 174.01(5)–177.4(3)°. These values are comparable to those of 175.40(6)° for P-Pd-P and 167.8(3)° for C-Pd-C in $[Pd_2(CN)_4(dppm)_2]$.[2b] The P-Pd-Pd angles in **1** and **2** are close to 90°. The C-Pd-Pd angles can be categorized into two sets. In **1**, the two sets of C-Pd-Pd angles are about 86.0 and 96.0°, which are close to 90.0°. However, the related values in **2** are 68.68(3)° and 117.30(3)°, that is, the PdP$_2$CN and Pd$_2$P$_2$ planes are not orthogonal to each other. The average Pd–C/Pd–P distances of 2.001(8)/2.345(2) Å in **1** and 2.003(1)/2.3135(4) Å in **2** are comparable to the average
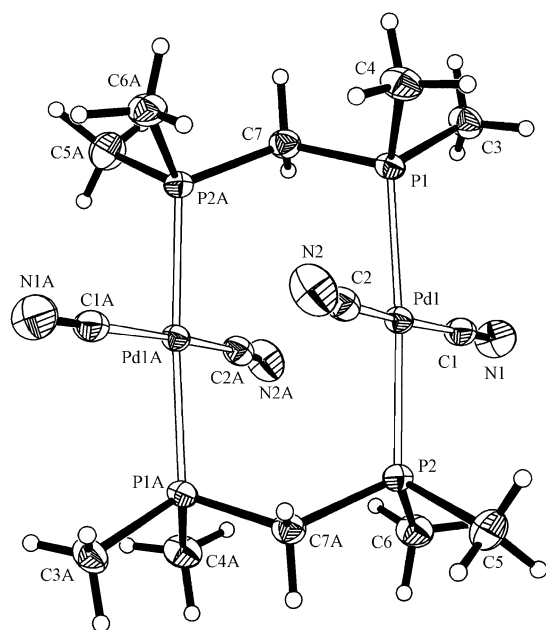
Figure 2. Structure of **2** (ORTEP plot: thermal ellipsoids at the 40% probability level).

Table 2. Selected bond lengths [Å] and angles [°] of **1** and **2**.

1·2.5 H$_2$O			
Pd1–P1	2.351(2)	Pd1–C1	2.001(7)
Pd1–P2	2.349(2)	Pd1–C2	2.013(7)
Pd2–P3	2.336(2)	Pd2–C3	2.015(9)
Pd2–P4	2.343(2)	Pd2–C4	1.975(8)
N1–C1	1.146(8)	N3–C3	1.14(1)
N2–C2	1.132(8)	N4–C4	1.143(9)
Pd1···Pd2	3.0432(7)		
Pd1-Pd2-P3	88.75(5)	Pd2-Pd1-C1	86.3(2)
Pd2-Pd1-P1	91.66(4)	Pd1-Pd2-C3	97.4(2)
Pd1-Pd2-P4	88.74(4)	Pd2-Pd1-C2	96.3(2)
Pd2-Pd1-P2	90.90(4)	Pd1-Pd2-C4	86.8(2)
P1-Pd1-P2	176.97(6)	P3-Pd2-P4	177.46(6)
P1-Pd1-C1	88.7(2)	P3-Pd2-C4	94.7(2)
C1-Pd1-C2	177.4(3)	C3-Pd2-C4	175.7(3)
2			
Pd1–P1	2.3123(4)	Pd1–P2	2.3147(4)
Pd1–C1	2.004(1)	Pd1–C2	2.002(1)
N1–C1	1.144(2)	N2–C2	1.132(2)
Pd1···Pd1A	3.307(4)		
C1-Pd1-C2	174.01(3)	P1-Pd1-P2	176.31(1)
N1-C1-Pd1	177.1(1)	N2-C2-Pd1	174.5(1)
C1-Pd1-P1	90.50(4)	C1-Pd1-P2	90.70(4)
C2-Pd1-P1	89.11(4)	C2-Pd1-P2	90.06(4)
P1-Pd1-Pd1A	91.0(3)	P2-Pd1-Pd1A	85.4(3)
C2-Pd1-Pd1A	68.68(3)	C1-Pd1-Pd1A	117.30(3)

values of 2.017(8) Å for Pd–C and 2.337(2) Å for Pd–P in [Pd$_2$(CN)$_4$(dppm)$_2$].[2b] The intramolecular Pd···Pd distances in **1** and **2** are 3.0432(7) and 3.307(4) Å, respectively.

Electronic spectra: The UV/Vis absorption spectra of **1**–**3** in CH$_3$OH at room temperature are depicted in Figure 3, and the spectral data, together with those of related complexes, are summarized in Table 3. Variable-temperature absorption spectra of **1** in CH$_3$OH are depicted in Figure 4. Complex **3** displays no detectable absorption at $\lambda > 300$ nm, while both **1** and **2** exhibit significant absorption at $300 < \lambda < 350$ nm. In CH$_3$OH solution at room temperature, complex **3** shows three absorption bands with λ_{max} at 205 ($\varepsilon = 19\,210$ dm^{3}mol^{-1}cm^{-1}), 228 (25 690), and 254 nm (28 770), and a shoulder at about 236 nm ($\varepsilon = 18\,690$ dm^{3}mol^{-1}cm^{-1}); complex **2** shows two absorption bands at $\lambda_{max} = 223$ ($\varepsilon = 37\,100$ dm^{3}mol^{-1}cm^{-1}) and 273 nm (12 640). Under the same conditions, the absorption spectrum of **1** is somewhat different from that of **2**; there is an intense absorption band at 239 nm ($\varepsilon = 34\,470$ dm^{3}mol^{-1}cm^{-1}) and a broad absorption consisting of three shoulder bands at

Figure 3. UV/Vis absorption spectra of **1**–**3** in CH$_3$OH at room temperature.

about 257 ($\varepsilon = 20\,000$ dm^{3}mol^{-1}cm^{-1}), 280 (11 560), and 310 nm (4060). The 273 nm band of **2** is similar to the 272 nm band of [Pd$_2$(CN)$_4$(dppm)$_2$];[2b] both are broad and

Table 3. Spectroscopic and photophysical properties of **1**–**3** and some related complexes.

| Complex	Medium	λ_{abs} [nm] (ε [dm^{3}mol^{-1}cm^{-1}])	λ_{em} [nm]/τ [µs]
[Pd$_2$(CN)$_4$(dcpm)$_2$] (**1**)	CH$_3$OH	203 (30 230), 239 (34 470), 257 (20 000), 280 (11 560), 310 (4060)	nonemissive
	CH$_2$Cl$_2$	237 (39 700), 257 (22 960), 285 (11 580), 310 (4890)	nonemissive
	solid		nonemissive
	solid[a]		503/19
	glass[a]		490/170
[Pd$_2$(CN)$_4$(dmpm)$_2$] (**2**)	CH$_2$Cl$_2$	230 (23 290), 275 (12 730)	nonemissive
	CH$_3$OH	223 (37 100), 273 (12 640)	nonemissive
	Solid[a]		493/1.7
trans-[Pd(CN)$_2$(PCy$_3$)$_2$] (**3**)	CH$_3$OH	205 (19 210), 228 (25 690), 236 (18 690), 254 (28 770)	nonemissive
[Pd$_2$(CN)$_4$(dppm)$_2$][b]	CH$_2$Cl$_2$	272 (52 000), 359 (500)	
trans-[Pd(CN)$_2$(PnBu$_3$)$_2$][c]	CH$_3$CN	200 (25 500), 221 (22 200), 228 (24 800), 244 (22 700)	
[Pd(DEPE)$_2$](PF$_6$)$_2$[c]	CH$_3$CN	211 (29 500), 221 (29 000), 242 (31 000), 253 (24 000)	

[a] At 77 K. [b] From ref. [2b]. [c] From ref. [22].
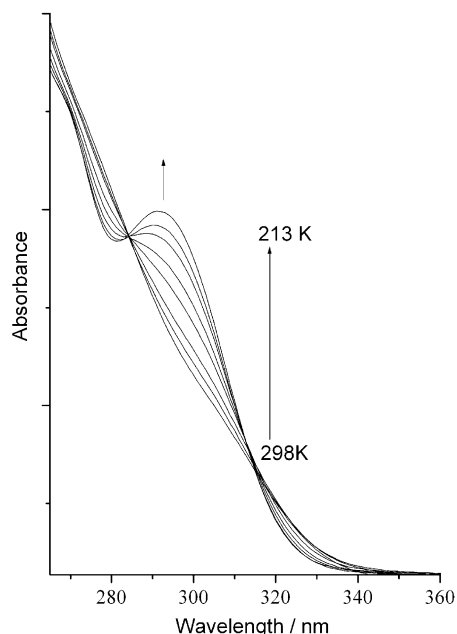
Figure 4. Variable-temperature UV/Vis absorption spectra of **1** in CH$_3$OH at 298, 288, 273, 263, 233, 223, and 213 K.

Figure 5. Excitation (——) and emission (••••) spectra of **1** in glassy solution (CH$_3$OH/EtOH 4/1 at 77 K) and emission spectra of **1** (----) and **2** (•–•–) in the solid state at 77 K.

unsymmetrical with absorption profile tails from the peak maxima to about 350 and 400 nm in **2** and [Pd$_2$(CN)$_4$(dppm)$_2$], respectively. We believe that these unsymmetrical absorption tails could have an electronic origin similar to that of the shoulder at about 310 nm in **1**.

As discussed below, the absorption spectrum of **1** is different from the excitation spectrum measured in glassy solution at 77 K at the 290–330 nm spectral region. This prompted us to record its absorption spectrum at low temperature. Spectra measured between 298 and 213 K are depicted in Figure 4. The structureless absorption at 290–350 nm at 298 K becomes a distinct absorption peak at $\lambda_{max} = 291$ nm at 213 K. We propose that the molecular structure of **1** at 213 K is different from that at room temperature; presumably, shortening of the Pd···Pd separation occurs at low temperature.

Emission spectra: Complexes **1** and **2** are nonemissive at room temperature but display emission at 77 K. Figure 5 shows the emission spectra of **1** and **2** in the solid state at 77 K and of **1** in glassy solution (CH$_3$OH/EtOH 4/1) at 77 K; the corresponding excitation spectrum monitored at the 490 nm emission of **1** in glassy solution at 77 K is also depicted. The photophysical data are summarized in Table 3. Complex **1** emits at 503 nm in the solid state (77 K) and at 490 nm in glassy solution (CH$_3$OH/EtOH 4/1, 77 K) with emission lifetimes in the microsecond regime. The excitation spectrum of **1** recorded in glassy solution features three distinct peak maxima at 242, 265, and 299 nm. This is comparable to the absorption spectrum of **1** in CH$_3$OH at 213 K. Complex **2** shows an emission at 493 nm with a lifetime of 1.7 μs in the solid state at 77 K.

Results of calculations: *[Pd$_2$(CN)$_4$(μ-H$_2$PCH$_2$PH$_2$)$_2$]*: Optimized geometrical parameters of the ground state of
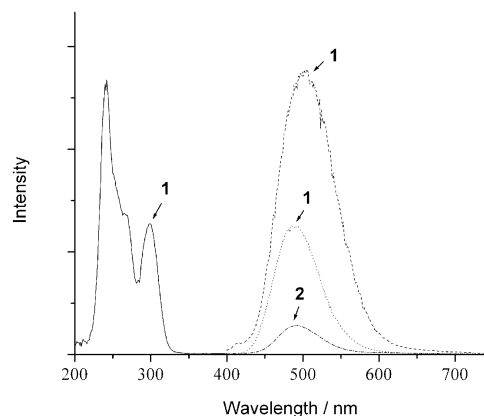
[Pd$_2$(CN)$_4$(μ-H$_2$PCH$_2$PH$_2$)$_2$] are summarized in Table 4. For both models A and B (C_2 and C_i symmetry, respectively; see Experimental Section), these parameters are similar, except that the optimized Pd···Pd distances are different (3.107 Å for model A and 3.355 Å for model B). The shorter optimized Pd···Pd distance of model A compared to model B is

Table 4. The main optimized geometrical parameters for [Pd$_2$(CN)$_4$(μ-H$_2$CH$_2$PH$_2$)$_2$].

	Calcd (A)	Exptl (**1**)	Calcd (B)	Exptl (**2**)
	Bond lengths [Å]			
Pd···Pd	3.107	3.0432(7)	3.355	3.307(4)
Pd–P	2.357	2.3447(2)	2.350	2.3135(4)
Pd–C	2.020	2.001(8)	2.020	2.003(1)
C–N	1.224	1.140(7)	1.224	1.138(2)
P–H	1.422		1.423	
C–H	1.104		1.106	
	Bond angles [°]			
P-Pd-Pd	90.5	90.01(4)	90.4	88.2(3)
C-Pd-Pd	93.8	91.7(2)	92.6	92.99(3)
P-Pd-P	179.1	177.21(6)	179.3	176.31(1)
C-Pd-C	172.4	176.35(3)	174.9	174.01(5)

consistent with the shorter Pd···Pd distance in **1** (pseudo-C_2 symmetry, 3.0432(7) Å) than in **2** (C_i symmetry, 3.307(4) Å), as revealed by X-ray structure determinations. The other optimized geometry parameters are also consistent with the corresponding bond lengths and angles of **1** and **2** in their X-ray crystal structures.

Compositions of high-lying occupied MOs that have 4d(Pd) parentage and of low-lying unoccupied MOs for models A and B are summarized in the Supporting Information. A simplified qualitative MO diagram is depicted in Figure 6. Because the electronic structures of the ground states of models A and B are similar (vide infra), and the C_i symmetry of model B facilitates assignment of the electronic transitions, we only performed CIS calculation on model B. The results are summarized in Table 5.

[{trans-[Pd(CN)$_2$(PH$_3$)$_2$]}$_2$]: Optimized geometrical parameters of *trans*-[Pd(CN)$_2$(PH$_3$)$_2$] and [{*trans*-[Pd(CN)$_2$(PH$_3$)$_2$]}$_2$] are listed in Table 6. For the monomer, structural data
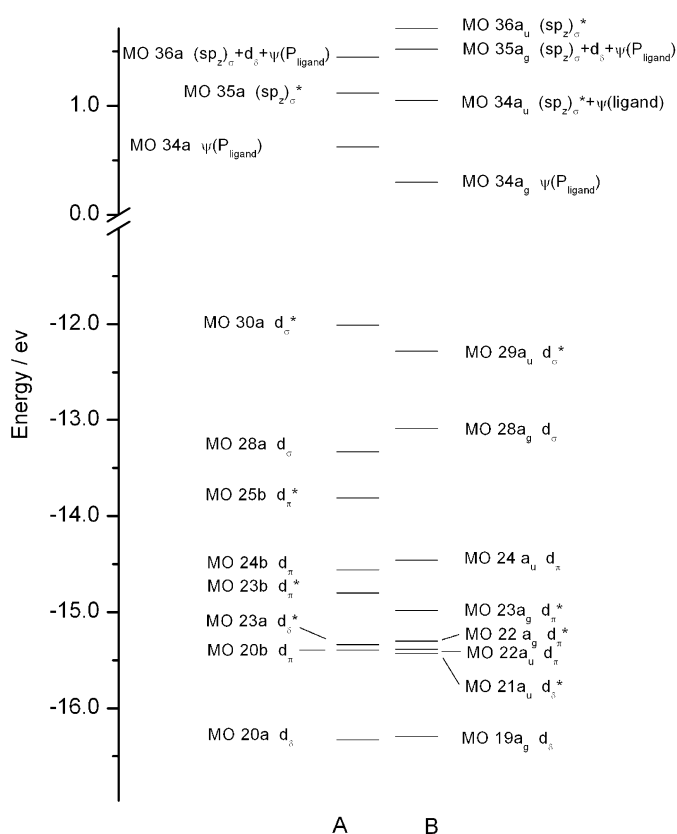
Figure 6. Simplified MO diagram showing the higher energy occupied MOs with large 4d(Pd) contributions for models A and B of [Pd$_2$(CN)$_4$(μ-H$_2$PCH$_2$PH$_2$)$_2$].

Table 6. Partial optimized structural parameters (bond lengths [Å] and angles [°] in *trans*-[Pd(CN)$_2$(PH$_3$)$_2$] and [{*trans*-[Pd(PH$_3$)$_2$(CN)$_2$]}$_2$] with b1 and b2 basis sets.

Monomer	b1	b2		
Pd–P	2.319	2.319		
Pd–C	1.992	1.982		
C–N	1.188	1.190		
P–H	1.421	1.423		
H-P-Pd	116.0	116.0		
dimer	b1, skewed	b1, eclipsed	b2, skewed	b2, eclipsed
Pd···Pd	3.221	3.602	3.186	3.470
Pd–C	1.991	1.995	1.978	1.983
Pd–P	2.322	2.303	2.313	2.293
C–N	1.190	1.189	1.192	1.191
P–H	1.415	1.416	1.412	1.418
P-Pd-Pd	94.1	95.2	95.6	97.3
C-Pd-Pd	91.0	91.0	90.7	91.9
H-P-Pd	116.7	117.6	116.5	117.3
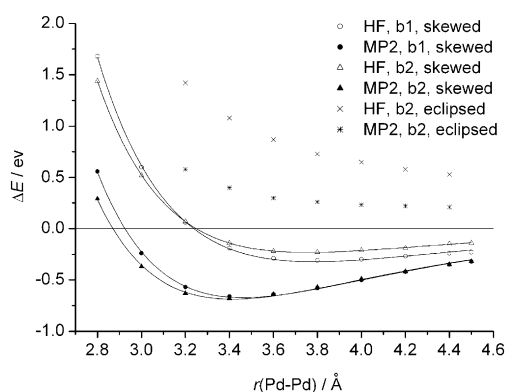
Figure 7. Interaction-energy curves of [{*trans*-[Pd(CN)$_2$(PH$_3$)$_2$]}$_2$], calculated by the CP method.

obtained with two different basis sets are similar. For the dimer, the optimized Pd···Pd distance in the skewed geometry calculated with the b1/b2 basis set is 0.38/0.28 Å shorter than those in the eclipsed geometry. This is consistent with the X-ray structural data: the Pd···Pd distance in **1** (3.0432(7) Å, the PdP$_2$(CN)$_2$ units are skewed, see above) is 0.26 Å shorter than that in **2** (3.307(4) Å, the PdP$_2$(CN)$_2$ units are eclipsed). The other optimized geometric parameters of the dimer [{*trans*-[Pd(CN)$_2$(PH$_3$)$_2$]}$_2$] with the two different basis sets are similar. In both the skewed and eclipsed dimers, the P-Pd-Pd angle is within 4–7° of 90°, and each *trans*-[Pd(CN)$_2$(PH$_3$)$_2$] unit is not coplanar. We used this optimized dimer structure to calculate the interaction energy. The calculated interaction energy curves are depicted in Figure 7.

Discussion

X-ray crystal structures: The Pd···Pd distances of 3.0432(7) Å in **1** and 3.307(4) Å in **2** are longer than those in the Pd$_2$ complexes mentioned in the Introduction. They are comparable to the values of 3.465(1) and 3.209(1) Å in discrete stacked molecules of *cis*-[Pd{*o*-C$_6$H$_4$N(O)O}$_2$],[20] and 3.276(1) Å in [Pd$_2$(CN)$_4$(dppm)$_2$].[2b] The Pd···Pd distance in **1**, however, is shorter than the intermolecular Pd···Pd separation of 3.37 Å in crystal chains of Ba[Pd(CN)$_4$]·4H$_2$O at room temperature[21] and the sum of the van der Waals radii (3.26 Å).[17]

Table 5. Calculated low-lying dipole-allowed electronic transitions of [Pd$_2$(CN)$_4$(μ-H$_2$PCH$_2$PH$_2$)$_2$] (model B).

Transition[a]	λ_{calcd} [nm]	Oscillator strength	Assignment	λ_{exptl} [nm] in [Pd$_2$(CN)$_4$(L)$_2$]		
				L = dcpm (**1**)	dmpm (**2**)	dppm
X^{1}A$_g$ → A^{1}A$_u$	303	0.0004				
28a$_g$ → 34a$_u$, 36a$_u$			d$_\sigma$ → [(sp)$_\sigma^*$ + Ψ(ligand)], (sp)$_\sigma^*$			
29a$_u$ → 34a$_g$, 35a$_g$			d$_\sigma^*$ → Ψ(P$_{ligand}$), [(sp)$_\sigma$ + d$_\delta$ + Ψ(P$_{ligand}$)]			
X^{1}A$_g$ → B^{1}A$_u$	289	0.0016		270–350	270–340	270–400
22a$_u$, 30a$_u$ → 35a$_g$			d$_\pi$, π(CN) → [(sp)$_\sigma$ + d$_\delta$ + Ψ(P$_{ligand}$)]			
23a$_g$, 33a$_g$ → 34a$_u$			d$_\pi^*$, π(CN) → [(sp)$_\sigma^*$ + Ψ(ligand)]			
23a$_g$, 33a$_g$ → 36a$_u$			d$_\pi^*$, π(CN) → (sp)$_\sigma^*$			

[a] The depicted MO transitions have |CI| coefficients > 0.2.

Spectroscopic properties: The absorption spectrum of **3** is similar to that of trans-[Pd(CN)$_2$(PnBu$_3$)$_2$][22] with a minor shift in absorption peak maximum; both complexes exhibit absorption at $\lambda < 300$ nm with ε values of $1.8-2.9 \times 10^4$ dm^3 mol^{-1} cm^{-1}, assigned to 4d(Pd) → [5p(Pd),3d(P),π*(CN)].[22] According to a previous theoretical investigation, the 3d(P) orbitals play no significant role in bonding.[23] However, the σ*(P−R) orbitals lie at relatively low energy and could act as acceptor orbitals.[23d]

We compared the absorption spectra of dinuclear Pd^{II} complexes with those of mononuclear congeners. The intense absorption band at 239 nm and the shoulder at about 257 nm in **1** are related to the Pd−P unit, since mononuclear Pd^{II} phosphane complexes display comparable bands; for example, [Pd(DEPE)$_2$](PF$_6$)$_2$[22] has absorption bands with $\lambda_{max} = 242$ ($\varepsilon = 31\,000$ dm^3 mol^{-1} cm^{-1}) and 253 nm (24 000). The band at 223 nm in **2** is also assigned to the absorption related to the Pd−P unit by comparison with absorptions at $\lambda_{max} = 228$ nm in **3**, 221 and 228 nm in trans-[Pd(CN)$_2$(PnBu$_3$)$_2$], and 221 nm in [Pd(DEPE)$_2$](PF$_6$)$_2$. The blue shift in absorption maximum from 239 nm in **1** to 223 nm in **2** appears to correlate with the corresponding decrease in Pd−P distances (av 2.345 Å in **1** and 2.314 Å in **2**). Here, the transition energy decreases as the Pd−P distance increases. A similar relationship was suggested for related trans-[Ni(CN)$_2$(phosphane)$_2$] and [Ni$_2$(CN)$_4$(phosphane)$_2$] complexes.[2f] The distinct intense absorption bands at $\lambda > 270$ nm with $\varepsilon > 10^4$ dm^3 mol^{-1} cm^{-1} in the dinuclear [Pd$_2$(CN)$_4$(phosphane)$_2$] complexes are absent in the absorption spectra of trans-[Pd(CN)$_2$(PCy$_3$)$_2$] and trans-[Pd(CN)$_2$(PnBu$_3$)$_2$]. Therefore, these absorption bands should be related to the Pd^{II}−Pd^{II} interaction.

The notable change in UV/Vis absorption spectrum of **1** at $\lambda = 280-350$ nm when the temperature decreases from 298 to 213 K (Figure 4) suggests structural nonrigidity of this complex. In solution, **1** may exist in several conformations with slightly different Pd···Pd separations at room temperature. This is supported by the broadening of its ^{31}P{^{1}H} NMR signal at lower temperatures. We propose fast dynamic interchange between different conformations of **1** at room temperature, and slowing of the exchange with decreasing temperature accounts for broadening of the ^{31}P{^{1}H} NMR signal. In **2** and [Pd$_2$(CN)$_4$(dppm)$_2$],[2b] the respective intense absorption bands with $\lambda_{max} = 273$ and 272 nm are broad with tailing extending to about 350 and 400 nm, respectively; they are similar to the distinct absorption of **1** at $\lambda_{max} = 291$ nm, recorded at 213 K. The red shift of these absorption bands relative to the absorption spectra of mononuclear congeners, together with their spectral profile and large ε_{max} values ($> 10^4$ dm^3 mol^{-1} cm^{-1}), are reminiscent of the $^1[nd_\sigma^* \rightarrow (n+1)p_\sigma]$ transitions of dinuclear d^8–d^8 and d^{10}–d^{10} complexes that have been shown to have weak metal–metal interactions. The red shift of these lower energy absorption bands from **2** ($\lambda_{max} = 273$ nm in CH$_3$OH) to **1** ($\lambda_{max} = 291$ nm in CH$_3$OH at 213 K) is consistent with a shorter Pd···Pd distance in the latter. We propose that these absorption bands have $^1(4d_\sigma^* \rightarrow 5p_\sigma)$ character. According to previous work on d^8–d^8 metal complexes,[1, 2] the strongly dipole allowed $nd_\sigma^* \rightarrow (n+1)p_\sigma$ transition is usually present as a distinct symmetric absorption

band with $\varepsilon_{max} > 10^4$ dm^3 mol^{-1} cm^{-1}. This is in contrast to the absorption spectrum of **1** at $\lambda = 280-350$ nm measured in CH$_2$Cl$_2$/CH$_3$OH, which exhibits overlapping dipole-allowed transitions. Indeed, ab initio calculations on the model [Pd$_2$(CN)$_4$(μ-H$_2$PCH$_2$PH$_2$)$_2$] revealed that the two low-lying dipole-allowed electronic transitions are close in energy and involve transitions from filled MOs that have 4d$_\sigma^*$ and 4d$_\pi$ character to unoccupied MOs that have (5s5p)$_\sigma$(Pd) and ligand character (see below). Thus, the absorption bands at $\lambda > 270$ nm in **1**, **2**, and [Pt$_2$(CN)$_4$(dppm)$_2$] are assigned to combinations of spin-allowed 4d$_\sigma^* \rightarrow$ (5s5p)$_\sigma$ and 4d$_\pi \rightarrow$ (5s5p)$_\sigma$ transitions.

These absorption bands are at higher energies than the 5d$_\sigma^* \rightarrow$ 6p$_\sigma$ transitions at 337 nm ($\varepsilon = 24\,100$ dm^3 mol^{-1} cm^{-1}) in [Pt$_2$(CN)$_4$(dcpm)$_2$], 328 nm ($\varepsilon = 24\,300$ dm^3 mol^{-1} cm^{-1}) in [Pt$_2$(CN)$_4$(dmpm)$_2$],[2f] and 324 nm ($\varepsilon = 10\,500$ dm^3 mol^{-1} cm^{-1}) in [Pt$_2$(CN)$_4$(dppm)$_2$].[2b] This is consistent with the larger $nd - (n+1)$p splitting for Pd^{II} than for Pt^{II}.[24] Unlike its platinum analogues, the spin-forbidden 4d$_\sigma^* \rightarrow$ (5s5p)$_\sigma$ and/or 4d$_\pi \rightarrow$ (5s5p)$_\sigma$ electronic transition in the [Pd$_2$(CN)$_4$(diphosphane)$_2$] complexes has not been recorded. Presumably, this is due to the smaller spin-orbital coupling constant of Pd^{II} ($\zeta_{4d} = 0.15\,\mu$m^{-1}) compared to Pt^{II} ($\zeta_{5d} = 0.35\,\mu$m^{-1}).[25]

The emissions of **1** and **2** at 77 K are phosphorescence due to their long lifetimes (in the microsecond regime). The excitation spectrum of **1** recorded in glassy solution (CH$_3$OH/ EtOH 4/1) at 77 K differs from its UV/Vis absorption spectrum at room temperature but is similar to that at 213 K. The distinct absorption band at 299 nm in glassy solution at 77 K is comparable to the absorption band at 291 nm in CH$_3$OH at 213 K. The emissions of **1** and **2** at about 490–500 nm have large Stokes shifts of 13 000–16 000 cm^{-1} relative to the low-energy absorption bands at 291 (at 213 K) and 273 nm in **1** and **2**, respectively. The Stoke shifts between the $^1[5d_\sigma^* \rightarrow 6p_\sigma]$ absorption and $^3[5d_\sigma^*6p_\sigma]$ emission energies are 7000–8000 cm^{-1} in [Pt$_2$(CN)$_4$(L)$_2$] (L = dcpm or dmpm)[2f] and [Pt$_2$(P$_2$O$_5$H$_2$)$_4$]$^{4-}$.[1] We propose that the emissions of **1** and **2** originate from an excited state that is not $^3[4d_\sigma^*(5s5p)_\sigma]$ in nature but could be attributed to $^3[4d_\pi(5s5p)_\sigma]$.

The emissions at about 490–500 nm in **1** and **2** at 77 K are comparable to the phosphorescence of Ba[Pd(CN)$_4$]·4H$_2$O at 512 nm at 7 K,[18] which was proposed to originate from intrachain Pd–Pd interaction. Note that intrachain Pd–Pd interaction could affect the energy of the [4d$_\pi$(5s5p)$_\sigma$] excited state.

Ground-state electronic structure: To probe the ground state metal–metal interaction in dinuclear Pd^{II} complexes, we analyzed the MO compositions in models A and B of [Pd$_2$(CN)$_4$(μ-H$_2$PCH$_2$PH$_2$)$_2$]. As shown in Figure 6 and Tables S1 and S2 (Supporting Information), the higher energy occupied MOs 31a to 33b (HOMO) in A and 30a$_g$ to 33a$_g$ (HOMO) in B are mainly CN ligand orbitals. The MOs 19a to 30a in A and 18a$_u$ to 29a$_u$ in B have large 4d(Pd) contributions. We only consider these two sets of MOs.

In model A with C_2 symmetry, the contributions of 4d(Pd) and ligand orbitals to MOs 19a or 21b are similar. These MOs are regarded as arising from Pd–ligand interactions. The MOs 20a, 20b, 21a, 22a, 23a, 23b, 24b, 25b, 28a, and 30a have

mainly contributions from 4d(Pd) orbitals and could be related to Pd–Pd interaction. The other MOs have little Pd character and are mainly ligand orbitals.

The MOs 20a and 23a are mainly composed of d$_{xy}$(Pd) (52.1 and 54.5%, respectively) with some d$_{x^2-y^2}$(Pd) character (18.6 and 11.1%, respectively) and are regarded as d$_\delta$ and d$_\delta^*$ orbitals. The MOs 20b and 23b with d$_{xz}$(Pd) contributions of 84.5 and 80.9%, respectively, are d$_\pi$ and d$_{\pi^*}$ orbitals. The MOs 24b and 25b with d$_{yz}$(Pd) contributions of 76.3 and 56.1%, respectively, are similarly assigned. The MO 25b with 38.8% P$_{ligand}$ contribution presumably results from d$_{yz}$(Pd)–P$_{ligand}$ interaction. The MOs 28a and 30a with d$_{z^2}$ contributions of 45.6 and 63.3%, respectively, are designated d$_\sigma$ and d$_\sigma^*$ orbitals. The MOs 21a and 22a have mixed d$_{z^2}$, d$_{x^2-y^2}$, and d$_{xy}$ characters; they are antibonding- and bonding like molecular orbitals.

Since all d$_\sigma$, d$_\pi$, d$_\delta$, d$_\delta$*, d$_\pi^*$, and d$_\sigma^*$ MOs are fully occupied, no net bonding interaction is expected. However, we note that there is some 5s(Pd) character in MOs 28a and 30a. The 5s(Pd) contribution to MO 28a (8.9%) is twice that in MO 30a (4.1%). Perhaps the slight outweighing of 5s(Pd) in bonding MO 28a relative to antibonding MO 30a results in weak Pd–Pd interaction. The calculated splittings of d$_\delta$/d$_\delta^*$, d$_\pi$/d$_\pi^*$, and d$_\sigma$/d$_\sigma^*$ orbitals for MOs 20a/23a, 20b/23b and 24b/25b, and 28a/30a are 0.99, 0.59 and 0.75, and 1.32 ev, respectively. These splittings are smaller than those of the Pt^{II} analogue [Pt$_2$(CN)$_4$(μ-H$_2$PCH$_2$PH$_2$)$_2$] (0.7–2.7 ev; the d$_\sigma$/d$_\sigma^*$ splitting is 2.66 ev).[2f] We infer that Pd–Pd interactions should be much weaker than Pt–Pt interactions.

For model B with C$_i$ symmetry, the electronic structure is similar to that of model A. The MOs 19a$_g$/21a$_u$, 22a$_u$/23a$_g$ and 22a$_g$/24a$_u$, and 28a$_g$/29a$_u$ are d$_\delta$/d$_\delta$*, d$_\pi$/d$_\pi^*$, and d$_\sigma$/d$_\sigma^*$ type orbitals with calculated splittings of 0.86, 0.40 and 0.84, and 0.81 eV, respectively. The main difference between A and B lies in the splittings of these metal–metal-bonding orbitals (see Figure 6). The shorter Pd···Pd separation in model A causes a slightly larger d$_\sigma$/d$_\sigma^*$ splitting.

Calculated electronic transitions: The two calculated low-lying dipole-allowed electronic transitions occur at 303 and 289 nm in [Pd$_2$(CN)$_4$(μ-H$_2$PCH$_2$PH$_2$)$_2$] (model B). As shown in Table 5, these are combinations of a number of orbital transitions with |CI| coefficients greater than 0.2.

For the 303 nm band, the 28a$_g$ → (34a$_u$, 36a$_u$) and 29a$_u$ → (34a$_g$, 35a$_g$) transitions have larger |CI| coefficients (>0.2). As noted above, MOs 28a$_g$ and 29a$_u$ are respectively d$_\sigma$ and d$_\sigma^*$ in nature. The MO 34a$_g$ is mainly the P$_{ligand}$ (74.6%) orbital with some p$_z$(Pd) parentage. The MO 34a$_u$ is a combination of (sp$_z$)$_\sigma^*$ with Ψ(P$_{ligand}$) and π*(CN), and has sp$_z$(Pd) and ligand (P$_{ligand}$ + CN) contributions of 65.8 and 34.2%, respectively. The MO 36a$_u$ is mainly an (sp$_z$)$_\sigma^*$ orbital, with an sp$_z$(Pd) contribution of 86.9%. The MO 35a$_g$ is a mixture of sp$_z$d$_{x^2-y^2}$(Pd) (53.9%) and P$_{ligand}$ (36.8%), which can be characterized as [(sp)$_\sigma$ + d$_\delta$ + Ψ(P$_{ligand}$)]. Therefore, the 303 nm band can be described as combination of d$_\sigma$ → {[(sp)$_\sigma^*$ + Ψ(ligand)],(sp)$_\sigma^*$} and d$_\sigma^*$ → {Ψ(P$_{ligand}$), [(sp)$_\sigma$ + d$_\delta$ + Ψ(P$_{ligand}$)]} transitions. The transition 29a$_u$ → 35a$_g$, which can be described as d$_\sigma^*$ → [(sp)$_\sigma$ + d$_\delta$ + Ψ(P$_{ligand}$)], has the largest |CI| coefficient (0.37) among all the orbital transitions

that contribute to the calculated 303 nm band. Therefore, the calculated transition band at 303 nm is not the same as the conventional metal-centered nd$_\sigma^*$ → $(n+1)$p$_\sigma$ electronic transition.

For the calculated band at 289 nm, the transitions (22a$_u$, 30a$_u$) → 35a$_g$, (23a$_g$, 33a$_g$) → 34a$_u$, and (23a$_g$, 33a$_g$) → 36a$_u$ have relatively large |CI| coefficients (>0.2). The MOs 22a$_u$ and 23a$_g$ are d$_\pi$ and d$_\pi^*$ orbitals, respectively. The MOs 30a$_u$ and 33a$_g$ are mainly π(CN) orbitals. Therefore, the calculated 289 nm band is assigned to a mixture of d$_\pi$, π(CN) → [(sp)$_\sigma$ + d$_\delta$ + Ψ(P$_{ligand}$)], d$_\pi^*$, π(CN) → [(sp)$_\sigma^*$ + Ψ(ligand)], and d$_\pi^*$, π(CN) → (sp)$_\sigma^*$ transitions.

In summary, the calculated absorption bands at 303 and 289 nm are combinations of many transitions involving MOs that have both metal and ligand components. Furthermore, the energy difference between these two calculated transition bands is small (1599 cm^{-1}). We attribute these two calculated transitions being the electronic origin of the absorption at $\lambda >$ 270 nm in **1**, **2**, and [Pd$_2$(CN)$_4$(dppm)$_2$].

Ground-state Pd^{II}–Pd^{II} interaction energy: The interaction energy curves obtained with the b1 and b2 basis sets are similar. As depicted in Figure 7, the interaction energy curves are attractive for the skewed dimer [{trans-[Pd(CN)$_2$-(PH$_3$)$_2$]}$_2$], but repulsive for the eclipsed dimer at both HF and MP2 levels (for simplification, only the results with the b2 basis set for eclipsed geometry are shown in Figure 7). Hence, Pd^{II}–Pd^{II} interaction in the ground state of **1**, which displays a skewed geometry for the two PdP$_2$(CN)$_2$ units, is confirmed. Complex **2** with the two PdP$_2$(CN)$_2$ units in an eclipsed geometry and a longer Pd···Pd separation does not have a Pd–Pd interaction.

The correlation attractive effects (at the MP2 level) are normal for weak interaction systems.[26] However, the attractive character at the HF level for the skewed dimer differs from previous reports on d^{10} metal dimers; for example, the calculated interaction energy curves for (ClAuPH$_3$)$_2$[27, 28] and (X-M-PH$_3$) (M = Cu, Ag, Au; X = H, Cl)[29] both exhibit repulsive trends at the HF level.

Here, for the skewed [{trans-[Pd(CN)$_2$(PH$_3$)$_2$]}$_2$] dimer, the electrostatic dipole–dipole interaction vanishes. The induction interaction is usually neglected since it is rarely the predominant source of attraction between molecules.[26] The HF interaction energy ΔE(HF) mainly results from short-range interaction, which arises from intermolecular Coulomb and exchange terms involving electrons on different monomers. Alternatively, the electron clouds of the two trans-[Pd(CN)$_2$(PH$_3$)$_2$] molecules interpenetrate each other, which brings about charge overlap and exchange effects.

The metallophilic attraction between monovalent d^{10} metal ions is referred to as a closed-shell interaction. However, the d^8 metal complexes of Pt^{II} and Pd^{II} are not good examples of closed-shell systems. The unoccupied valence nd shell is liable to hybridize with the upper $(n+1)$s,p shell. Hence, the interaction between d^8 metal ions such as Pd^{II} cannot be described by correlation effects alone.

The well depth of the interaction energy curve for the skewed structure is pronounced, with a ΔE value of about -0.67 eV (-15.5 kcal mol^{-1}) at r(Pd–Pd) = 3.46 Å and

−0.69 eV (−15.9 kcal mol⁻¹) at r(Pd−Pd) = 3.41 Å at the MP2 level, and −0.32 eV (−7.4 kcal mol⁻¹) at r(Pd−Pd) = 3.78 Å and −0.23 eV (−5.3 kcal mol⁻¹) at r(Pd−Pd) = 3.76 Å at the HF level with the b1 and b2 basis sets, respectively. However, the values of −0.67 or −0.69 eV at the MP2 level cannot be regarded as the bonding interaction energy of Pd^{II}−Pd^{II} because the curves cannot reach the zero point even at r(Pd−Pd) = 4.5 Å (ΔE = −0.32, −0.23 eV at the MP2 and HF levels with b1, −0.32, −0.14 eV at the MP2 and HF levels with b2). We assume that Pd^{II}−Pd^{II} orbital interaction should vanish at r(Pd−Pd) = 4.5 Å (long Pd···Pd separation), and this assumption should be reasonable because the attractive character of the ΔE value at r(Pd−Pd) ≥ 4.5 Å can only originate from the long-range van der Waals interaction, which arises from electrostatic, inductive, and dispersion interactions [see Experimental Section, Eq. (3)] and should not have contributions from metal–metal bonding. Under this assumption, the well depth can be corrected by the ΔE value at r(Pd−Pd) = 4.5 Å, and the corrected values are −0.35 eV (−8.1 kcal mol⁻¹, b1) and −0.37 eV (−8.5 kcal mol⁻¹, b2) at the MP2 level, and −0.09 eV (−2.1 kcal mol⁻¹) at the HF level. These corrected values can be compared to the weak cuprophilic and argentophilic interaction energies of ca. 4–9 kcal mol⁻¹ calculated by Stoll et al.[29] and Schwerdtfeger et al.[30] for a number of model compounds. These results indicate that Pd^{II}−Pd^{II} interaction is weaker than aurophilicity; the well-documented Au^{I}−Au^{I} interaction energy can be as large as 7–10 kcal mol⁻¹.[31] Alvarez et al.[32] reported metal–metal bonding energies of 9.1 and 19.9 kcal mol⁻¹ in [{PtCl₂(CO)₂}₂] and [{trans-[PtCl₂{HNCH(OH)}₂]}₂]. Our calculated value for [{trans-[Pd(CN)₂(PH₃)₂]}₂] is much smaller than these.

We note that the calculated r_{eq}(Pd−Pd) of 3.41 or 3.46 Å at the MP2 level is longer than the Pd···Pd separation of 3.0432(7) Å in **1** and the optimized Pd···Pd distance of ca. 3.2 Å in the skewed [{trans-[Pd(CN)₂(PH₃)₂]}₂]. This may have several reasons. First, the two Pd atoms in the theoretical model are unbridged, whereas those in **1** are bridged, and the presence of a bridging group will shorten the metal–metal distance. Second, the interaction-energy curve does not describe the absolute minima on the interaction-energy surface of [{trans-[Pd(CN)₂(PH₃)₂]}₂], since only the coordinate of the Pd−Pd distance was varied during calculation. Furthermore, the Pd^{II}−Pd^{II} interaction can occur over a range of Pd···Pd separations. At r(Pd−Pd) = 3.0 Å (the Pd···Pd separation in **1**), the interaction energy curve at the MP2 level is attractive. The equilibrium separation is also affected by the ligands ligating the metal atoms. Metal complexes with bulky ligands usually exhibit long equilibrium metal–metal distances, as suggested by Pyykkö et al..[28] Although the results of the calculation provide qualitative evidence for this, the conclusion on the attractive interaction in the skewed dimer is confirmed.

Conclusion

We have examined the Pd^{II}−Pd^{II} interaction in dinuclear [Pd₂(CN)₄(μ-diphosphane)₂] complexes by spectroscopy and ab initio calculations. The intense absorption bands at λ > 270 nm in **1**, **2**, and [Pd₂(CN)₄(dppm)₂] could be related to Pd^{II}−Pd^{II} interactions. Weak but attractive Pd^{II}−Pd^{II} interaction in the ground state was verified by calculations at the MP2 level.

Experimental Section

General: The starting materials [PdCl₂(L)] (L = dcpm, dmpm) were prepared following a procedure similar to that for [PdCl₂(dppm)]. [19] The mononuclear complex **3** was prepared by a method similar to that for *trans*-[Pd(CN)₂(PnBu₃)₂].[22] ¹H and ³¹P NMR spectra were recorded on a Bruker DRX-500 multinuclear FT-NMR spectrometer. Chemical shifts (δ/ppm) were reported relative to tetramethylsilane (¹H NMR) and 85% H₃PO₄ (³¹P NMR). Infrared spectra were obtained on a Bio-Rad FTS-165 spectrometer. Room-temperature UV/Vis spectra were obtained on a Hewlett-Packard 8453 diode-array spectrophotometer, and the variable-temperature spectra were recorded on a Perkin Elmer Lambda 900 spectrophotometer. Positive-ion FAB mass spectra were recorded on a Finnigan MAT95 mass spectrometer. Elemental analyses were performed by the Institute of Chemistry, the Chinese Academy of Sciences.

[Pd₂(CN)₄(μ-dcpm)₂] (1): [PdCl₂(dcpm)] (0.130 g, 0.22 mmol) was suspended in CH₃OH (10 mL). A methanolic solution (15 mL) of NaCN (0.024 g, 0.49 mmol) was added dropwise to give a colorless solution. After reaction for 10 h, the solvent was removed and a white solid was obtained, which was washed with water and dried. Yield: 0.09 g (70%). Crystals for X-ray crystallography were obtained by slow evaporation of a CH₃OH solution. ¹H NMR (CDCl₃): δ = 2.82 (m, CH₂), 1.25–2.50 ppm (m, Cy); ³¹P{¹H} NMR (CD₃OD): δ = 28.59 (s, 20°C); 28.49 (s, 0°C); 28.37 (s, −20°C), 28.26 (−40°C); 28.09 ppm (s, −60°C); IR (KBr disk): $\tilde{\nu}$ = 2125 cm⁻¹ (C≡N); MS (FAB, +ve): m/z: 1108 [M − CN]⁺; elemental analysis (%) calcd for C₅₄H₉₂N₄P₄Pd₂ · H₂O (1152.10): C 56.30, H 8.22, N 4.86; found: C 56.03, H 8.50, N 4.53.

[Pd₂(CN)₄(μ-dmpm)₂] (2): This complex was prepared by a method similar to that for **1**. Yield: 82%. ¹H NMR (CDCl₃): δ = 1.98 (m, CH₂); 1.51–1.54 ppm (CH₃); ³¹P{¹H} NMR (CDCl₃/CD₃OD): δ = −5.13 (s, 20°C); −4.97 (s, 0°C); −4.79 (s, −20°C); −4.60 (s, −40°C); −4.38 ppm (s, −60°C); IR (KBr disk): $\tilde{\nu}$ = 2124 cm⁻¹ (C≡N); MS (FAB, +ve): m/z: 589 [M]⁺; elemental analysis (%) calcd for C₁₄H₂₈N₄P₄Pd₂ (589.14): C 28.54, H 4.79, N 9.51; found: C 28.57, H 4.80, N 9.50.

***trans*-[Pd(CN)₂(PCy₃)₂] (3)**: A solution of [PdCl₂(PCy₃)₂] (0.120 g, 0.16 mmol) and NaCN (0.015 g, 0.30 mmol) in methanol (20 mL) was refluxed for 10 h to give a colorless solution. After removal of solvent, the white product was washed with water and dried. Yield: 0.11 g (87%). ¹H NMR: (CDCl₃): δ = 1.20–2.75 ppm (m, Cy); ³¹P{¹H} NMR (CDCl₃): δ = 40.36 ppm (s); IR (KBr): $\tilde{\nu}$ = 2124 cm⁻¹ (C≡N); MS (+ve FAB): m/z: 719 [M]⁺; elemental analysis (%) calcd for C₃₈H₆₆N₂P₂Pd (719.31): C 63.45, H 9.25, N 3.89; found: C 63.65, H 9.49, N 3.22.

Computational details: All calculations were performed on the High Performance Computing Cluster with the Gaussian 98 program package.[33]

[Pd₂(CN)₄(μ-H₂PCH₂PH₂)₂]: In this work, [Pd₂(CN)₄(μ-H₂PCH₂PH₂)₂] was used as a model of **1** and **2** for calculations. The ground-state structures were partially optimized at the second-order Møller–Plesset (MP2) level.[34] Based on the optimized ground state structures, single-excitation configuration interaction (CIS)[35] calculations for low-lying dipole-allowed electronic transitions were undertaken. In crystalline form, **1** has pseudo-C_2 symmetry, and **2** has C_i symmetry. Therefore, the model molecule [Pd₂(CN)₄(μ-H₂PCH₂PH₂)₂] was optimized with C_2 (model A) and C_i (model B) symmetry, respectively. In the model molecule, the z axis is coincident with the Pd−Pd vector, and the y axis is set parallel to the C−C vector of two CH₂ units. For the sake of simplicity, we only performed CIS calculations on [Pd₂(CN)₄(μ-H₂PCH₂PH₂)₂] with C_i symmetry. In the calculations, the quasirelativistic pseudopotentials of Pd and P atoms proposed by Hay and Wadt[36] with 18 and 5 valence electrons (VE), respectively, were employed. The LANL2DZ basis sets were adopted for all atoms.

[{*trans*-[Pd(PH₃)₂(CN)₂]}₂]: The Pd^{II}–Pd^{II} interaction of ground state [{*trans*-[Pd(CN)₂(PH₃)₂]}₂] was calculated. Two sets of basis sets were used for the Pd atom: one (set b1) is the LANL2DZ set used for [Pd₂(CN)₄(μ-H₂PCH₂PH₂)₂] but with addition of a diffuse f-polarization function (α_f = 0.14), and the other (set b2) is the 18-VE quasirelativistic (QR) pseudopotential and basis set of Andrae[37] with an additional diffuse f-polarization function (α_f = 0.10). The diffuse f orbital exponents were obtained by maximizing the Pd(0) MP2 electric-dipole polarizability. For P atoms, the LANL2DZ basis set and pseudopotential was used. A d-polarization function (α_d = 0.334[38]) was added. For C, N, and H atoms, the standard 6-31g* basis sets were used.

The structures of *trans*-[Pd(CN)₂(PH₃)₂] (C_{2h} symmetry) and [{*trans*-[Pd(CN)₂(PH₃)₂]}₂] were optimized at the MP2 level. The dimeric [{*trans*-[Pd(CN)₂(PH₃)₂]}₂] molecule was arranged to have either an eclipsed or a skewed geometry (Scheme 1), and its structure was optimized in each case.
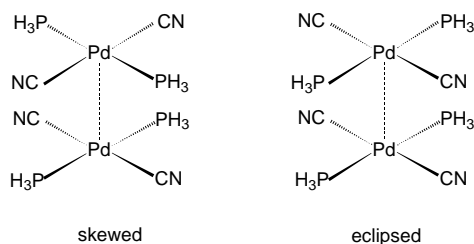
Scheme 1. Structures of [{*trans*-[Pd(CN)₂(PH₃)₂]}₂].

The P-Pd-Pd and C-Pd-Pd angles were not kept constant but optimized. The optimized *trans*-[Pd(CN)₂(PH₃)₂] and [{*trans*-[Pd(CN)₂(PH₃)₂]}₂] structures were used for calculating the Pd^{II}–Pd^{II} interaction energy by varying the r(Pd–Pd) value and maintaining the other structure parameters. The interaction energies were obtained according to Equation (1); the counterpoise (CP) corrections for basis-set superposition errors (BSSE)[39] were taken into account.

$$\Delta E_{cp} = E_{Pd2}^{(Pd2)} - 2E_{Pd}^{(Pd2)} = V_{int}(r) \qquad (1)$$

The term ΔE_{cp} is the interaction energy with CP corrections, $E_{Pd2}^{(Pd2)}$ is the energy of the [{*trans*-[Pd(CN)₂(PH₃)₂]}₂] dimer, which was calculated on the optimized geometry with varying r(Pd–Pd) distances, and $E_{Pd}^{(Pd2)}$ is the energy of *trans*-[Pd(CN)₂(PH₃)₂] monomer at different r(Pd–Pd) values, calculated by the CP method[39] (see Scheme 2).

An alternative partitioning of the interaction energy of Equation (1) is given in Equation (2), where ΔE(HF) is the interaction energy evaluated from self-consistent field (SCF) calculations at the Hartree–Fock (HF) level, and $\Delta E^{(2)}$ is the second-order correlation interaction energy.

$$\Delta E(MP2) = \Delta E(HF) + \Delta E^{(2)} = V_{int}(r) \qquad (2)$$

The intermolecular potential V_{int} can be partitioned into short-range (V_{short}), electrostatic (V_{elect}), induction (V_{ind}), and dispersion (V_{disp}) contributions[26] [Eq. (3)].

$$V_{int} = V_{short} + V_{elect} + V_{ind} + V_{disp} \qquad (3)$$

It is common practice to associate the HF term ΔE(HF) with the sum of V_{short}, V_{elect}, and V_{ind}, while the $\Delta E^{(2)}$ [Eq. (2)] electron-correlation term is associated with dispersion (V_{disp}).[26]

We fitted the calculated interaction energy points using the Morse type potential, as described by Equation (4).[40]

$$\Delta E(r) = D\{[1 - \exp(-a[r - r_0])]^2 - 1\} \qquad (4)$$

Photophysical measurements: Steady-state emission and excitation spectra at room temperature and 77 K were obtained on a Spex 1681 Flurolog-2 Model F111AI fluorescence spectrophotometer equipped with a Hamamatsu R928 PMT detector. The spectra at 77 K in the solid state and at 77 K in glassy solution in MeOH/EtOH (4/1) were recorded on samples in quartz
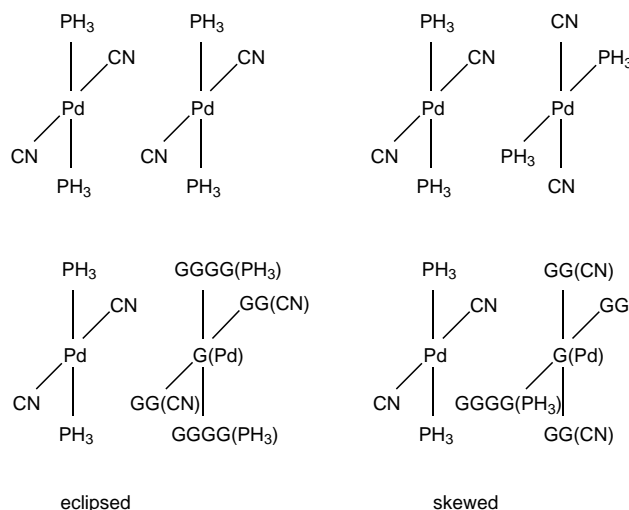
Scheme 2. Schematic structures for calculating interaction-energy curves by the CP method. G denotes ghost atoms, that is, the Gaussian basis functions at the corresponding position were taken into account but the charge was zero. The upper structures are for the dimer, and the lower for the monomer.

tubes immersed in a quartz-wall optical Dewar flask filled with liquid nitrogen. For measurements of solution emission spectra at room temperature, the solutions were subjected to four freeze/pump/thaw cycles prior to measurements. The emission lifetime was measured by time-resolved photon counting with Multi-Channel Scaler/Averager Model SR430.

X-ray structure determinations: Graphite-monochromatized Mo$_{K\alpha}$ radiation (λ = 0.71073 Å) was used. For **1** · 2.5 H₂O, crystal data were collected at 301 K on an MAR diffractometer with a 300 mm image-plate detector. The images were interpreted and intensities integrated by using the program DENZO.[41] The structure was solved by Patterson methods, expanded by Fourier methods (PATTY[42]), and refined by full-matrix least-squares methods (TeXsan[43]) on a Silicon Graphics Indy computer. The crystallographic asymmetric unit consists of one formula unit with O(3) of the third water molecule at a special position. Three of the C atoms of one of the cyclohexyl rings bonded to P(4) were placed at two alternate positions such that C(52), C(52′), C(53), C(53′), C(54) and C(54′) all had half occupancy. In the least-squares refinement, 64 non-H atoms were refined anisotropically, the disordered C atoms were refined isotropically, and 81 H atoms at calculated positions with thermal parameters equal to 1.3 times that of the attached C atoms were not refined. H atoms of the disordered cyclohexyl ring and the water molecules were not included in the calculation. For **2**, the diffraction experiment was performed at 294 K on a Bruker SMART CCD diffractometer. The crystal structure was determined by direct methods and refined by full-matrix least-squares methods on F^2 (SHELXL97[44]) on a PC.

CCDC-200046 (**1**) and CCDC-200047 (**2**) contain the supplementary crystallographic data for this paper. These data can be obtained free of charge via www.ccdc.cam.ac.uk/conts/retrieving.html (or from the Cambridge Crystallographic Data Centre, 12 Union Road, Cambridge CB2 1EZ, UK; fax: (+44) 1223–336–033; or deposit@ccdc.cam.uk).

Acknowledgement

[1] D. M. Roundhill, H. B. Gray, C.-M. Che, *Acc. Chem. Res.* **1989**, *22*, 55–61.

[2] a) C.-M. Che, V. W.-W. Yam, W.-T. Wong, T.-F. Lai, *Inorg. Chem.* **1989**, *28*, 2908 – 2910; b) H.-K. Yip, T.-F. Lai, C.-M. Che, *J. Chem. Soc. Dalton Trans.* **1991**, 1639 – 1641; c) J. A. Bailey, V. M. Miskowski, H. B. Gray, *Inorg. Chem.* **1993**, *32*, 369 – 370; d) J. A. R. Navarro, M. A. Romero, J. M. Salas, M. Quirós, J. E. Bahraoui, J. Molina, *Inorg. Chem.* **1996**, *35*, 7829 – 7835; e) S.-W. Lai, M. C.-W. Chan, T.-C. Cheung, S.-M. Peng, C.-M. Che, *Inorg. Chem.* **1999**, *38*, 4046 – 4055; f) B.-H. Xia, C.-M. Che, D. L. Phillips, K.-H. Leung, K.-K. Cheung, *Inorg. Chem.* **2002**, *41*, 3866 – 3875.

[3] a) K. R. Mann, J. G. Gordon, II, H. B. Gray, *J. Am. Chem. Soc.* **1975**, *97*, 3553 – 3555; b) R. F. Dallinger, V. M. Miskowski, H. B. Gray, W. H. Woodruff, *J. Am. Chem. Soc.* **1981**, *103*, 1595 – 1596; c) S. F. Rice, H. B. Gray, *J. Am. Chem. Soc.* **1981**, *103*, 1593 – 1595; d) S. F. Rice, S. J. Milder, H. B. Gray, *Coord. Chem. Rev.* **1982**, *43*, 349 – 354; e) J. L. Marshall, S. R. Stobart, H. B. Gray, *J. Am. Chem. Soc.* **1984**, *106*, 3027 – 3029; f) S. F. Rice, V. M. Miskowski, H. B. Gray, *Inorg. Chem.* **1988**, *27*, 4704 – 4708; g) J. L. Marshall, M. D. Hopkins, V. M. Miskowski, H. B. Gray, *Inorg. Chem.* **1992**, *31*, 5034 – 5040.

[4] D. C. Smith, H. B. Gray, *Coord. Chem. Rev.* **1990**, *100*, 169 – 181.

[5] a) C.-M. Che, L. G. Butler, H. B. Gray, R. M. Crooks, W. H. Woodruff, *J. Am. Chem. Soc.* **1983**, *105*, 5492 – 5494; b) D. C. Smith, V. M. Miskowski, W. R. Mason, H. B. Gray, *J. Am. Chem. Soc.* **1990**, *112*, 3759 – 3767; c) D. C. Smith, V. M. Miskowski, W. R. Mason, H. B. Gray, *J. Am. Chem. Soc.* **1990**, *112*, 3759 – 3767; d) J. L. Marshall, M. D. Hopkins, V. M. Miskowski, H. B. Gray, *Inorg. Chem.* **1992**, *31*, 5034 – 5040; e) V. M. Miskowski, S. F. Rice, H. B. Gray, S. J. Milder, *J. Phys. Chem.* **1993**, *97*, 4277 – 4283; f) V. M. Miskowski, S. F. Rice, H. B. Gray, R. F. Dallinger, S. J. Milder, M. G. Hill, C. L. Exstrom, K. R. Mann, *Inorg. Chem.* **1994**, *33*, 2799 – 2807; g) R. F. Dallinger, M. J. Carlson, V. M. Miskowski, H. B. Gray, *Inorg. Chem.* **1998**, *37*, 5011 – 5013; h) K. H. Leung, D. L. Phillips, C.-M. Che, V. M. Miskowski, *J. Raman Spectrosc.* **1999**, *30*, 987 – 993.

[6] M. Bonamico, G. Dessy, V. Fares, *J. Chem. Soc. Dalton Trans.* **1977**, 2315 – 2319.

[7] M. Corbett, B. F. Hoskins, N. J. McLeod, B. P. O'Day, *Aust. J. Chem.* **1975**, *28*, 2377 – 2392.

[8] O. Piovesana, C. Bellitto, A. Flamini, P. F. Zanazzi, *Inorg. Chem.* **1979**, *18*, 2258 – 2265.

[9] W. Clegg, C. D. Garner, M. H. Al-Samman, *Inorg. Chem.* **1982**, *21*, 1897 – 1901.

[10] M. Kubiak, *Acta Crystallogr. Sect. C* **1985**, *41*, 1288 – 1290.

[11] D. P. Bancroft, F. A. Cotton, L. R. Falvello, W. Schwotzer, *Inorg. Chem.* **1986**, *25*, 1015 – 1021.

[12] K. Umakoshi, I. Kinoshita, S. Ooi, *Inorg. Chem. Acta* **1987**, *127*, L41 – L42.

[13] F. A. Cotton, M. Matusz, R. Poli, X. Feng, *J. Am. Chem. Soc.* **1988**, *110*, 1144 – 1154.

[14] J. L. García-Ruano, I. López-Solera, J. R. Masaguer, C. Navarro-Ranninger, J. H. Rodríguez, S. Martínez-Carrera, *Organometallics* **1992**, *11*, 3013 – 3018.

[15] B.-C. Tzeng, S.-C. Chan, M. C. W. Chan, C.-M. Che, K.-K. Cheung, S.-M. Peng, *Inorg. Chem.* **2001**, *40*, 6699 – 6704.

[16] J. S. Miller, A. J. Epstein, *Prog. Inorg. Chem.* **1976**, *20*, 1 – 151.

[17] A. Bondi, *J. Phys. Chem.* **1964**, *68*, 441 – 451.

[18] W. D. Ellenson, A. K. Viswanath, H. H. Patterson, *Inorg. Chem.* **1981**, *20*, 780 – 783.

[19] a) G. R. Cooper, A. T. Hutton, C. R. Langrick, D. M. McEwan, P. G. Pringle, B. L. Shaw, *J. Chem. Soc. Dalton Trans.* **1984**, 855 – 862; b) F. S. M. Hassan, D. P. Markham, P. G. Pringle, B. L. Shaw, *J. Chem. Soc. Dalton Trans.* **1985**, 279 – 283.

[20] J. Vicente, M. T. Chicote, J. Martín, M. Artigao, X. Solans, M. Font-Altaba, M. Aguiló, *J. Chem. Soc. Dalton Trans.* **1988**, 141 – 148.

[21] D. Rassenfosse, J. Piérard, *Bull. Soc. Roy. Sci. Liége* **1938**, 74 – 79.

[22] J. M. Solar, M. A. Ozkan, H. Isci, W. R. Mason, *Inorg. Chem.* **1984**, *23*, 758 – 764, and references therein.

[23] a) S.-X. Xiao, W. C. Trogler, D. E. Ellis, Z. Berkovitch-Yellin, *J. Am. Chem. Soc.* **1983**, *105*, 7033 – 7037; b) D. S. Marynick, *J. Am. Chem. Soc.* **1984**, *106*, 4064 – 4065; c) G. Pacchioni, P. S. Bagus, *Inorg. Chem.* **1992**, *31*, 4391 – 4398; d) D. G. Gilheany, *Chem. Rev.* **1994**, *94*, 1339 – 1374.

[24] W. R. Mason, III, H. B. Gray, *J. Am. Chem. Soc.* **1968**, *90*, 5721 – 5729.

[25] J. S. Griffith, *The Theory of Transition Metal Ions*, Cambridge University Press, London, **1964**, Tables A6.1 – A6.3.

[26] A. D. Buckingham, P. W. Fowler, J. M. Hutson, *Chem. Rev.* **1988**, *88*, 963 – 988.

[27] P. Pyykkö, Y. Zhao, *Angew. Chem.* **1991**, *103*, 622 – 623; *Angew. Chem. Int. Ed. Engl.* **1991**, *30*, 604 – 605.

[28] P. Pyykkö, N. Runeberg, F. Mendizabal, *Chem. Eur. J.* **1997**, *3*, 1451 – 1457.

[29] L. Magnko, M. Schweizer, G. Rauhut, M. Schütz, H. Stoll, H.-J. Werner, *Phys. Chem. Chem. Phys.* **2002**, *4*, 1006 – 1013.

[30] H. L. Hermann, G. Boche, P. Schwerdtfeger, *Chem. Eur. J.* **2001**, *7*, 5333 – 5342.

[31] H. Schmidbaur, *Chem. Soc. Rev.* **1995**, 391 – 400.

[32] J. J. Novoa, G. Aullón, P. Alemany, S. Alvarez, *J. Am. Chem. Soc.* **1995**, *117*, 7169 – 7171.

[33] Gaussian 98, Revision A.11.3, M. J. Frisch, G. W. Trucks, H. B. Schlegel, G. E. Scuseria, M. A. Robb, J. R. Cheeseman, V. G. Zakrzewski, J. A. Montgomery, Jr., R. E. Stratmann, J. C. Burant, S. Dapprich, J. M. Millam, A. D. Daniels, K. N. Kudin, M. C. Strain, O. Farkas, J. Tomasi, V. Barone, M. Cossi, R. Cammi, B. Mennucci, C. Pomelli, C. Adamo, S. Clifford, J. Ochterski, G. A. Petersson, P. Y. Ayala, Q. Cui, K. Morokuma, N. Rega, P. Salvador, J. J. Dannenberg, D. K. Malick, A. D. Rabuck, K. Raghavachari, J. B. Foresman, J. Cioslowski, J. V. Ortiz, A. G. Baboul, B. B. Stefanov, G. Liu, A. Liashenko, P. Piskorz, I. Komaromi, R. Gomperts, R. L. Martin, D. J. Fox, T. Keith, M. A. Al-Laham, C. Y. Peng, A. Nanayakkara, M. Challacombe, P. M. W. Gill, B. Johnson, W. Chen, M. W. Wong, J. L. Andres, C. Gonzalez, M. Head-Gordon, E. S. Replogle, J. A. Pople, Gaussian, Inc., Pittsburgh PA, **2002**.

[34] C. Møller, M. S. Plesset, *Phys. Rev.* **1934**, *46*, 618 – 622.

[35] J. B. Foresman, M. Head-Gordon, J. A. Pople, M. J. Frisch, *J. Chem. Phys.* **1992**, *96*, 135 – 149.

[36] a) P. J. Hay, W. R. Wadt, *J. Chem. Phys.* **1985**, *82*, 299 – 310; b) W. R. Wadt, P. J. Hay, *J. Chem. Phys.* **1985**, *82*, 284 – 298.

[37] D. Andrae, U. Häußermann, M. Dolg, H. Stoll, H. Preuß, *Theor. Chim. Acta* **1990**, *77*, 123 – 141.

[38] C. E. Check, T. O. Faust, J. M. Bailey, B. J. Wright, T. M. Gilbert, L. S. Sunderlin, *J. Phys. Chem. A* **2001**, *105*, 8111 – 8116.

[39] S. F. Boys, F. Bernardi, *Mol. Phys.* **1970**, *19*, 553.

[40] P. Spuhler, M. C. Holthausen, D. Nachtigallová, P. Nachtigall, J. Sauer, *Chem. Eur. J.* **2002**, *8*, 2099 – 2115.

[41] DENZO: D. Gewrith, Z. Otwinowski, W. Minor, The HKL Manual— A Description of Programs DENZO, XDISPLAY, and SCALEPACK, Yale University, New Haven, **1995**.

[42] PATTY: P. T. Beurskens, G. Admiraal, G. Beurskens, W. P. Bosman, S. Garcia-Granda, R. O. Gould, J. M. M. Smits, C. Smykalla, The DIRDIF Program System, Technical Report of the Crystallography Laboratory, University of Nijmegen, The Netherlands, **1992**.

[43] TeXsan: Crystal Structure Analysis Package, Molecular Structure Corporation, The Woodlands, Texas, **1985**, **1992**.

[44] SHELXL97: G. M. Sheldrick, SHELXL97 Programs for Crystal Structure Analysis (Release 97-2), University of Göttingen, Germany, **1997**.